Published in final edited form as:
Phys Med Biol. 2013 March 7; 58(5): . doi:10.1088/0031-9155/58/5/N59.

COMPUTATIONAL LYMPHATIC NODE MODELS IN PEDIATRIC AND ADULT HYBRID PHANTOMS FOR RADIATION DOSIMETRY

Choonsik Lee, **Stephanie Lamart**, and **Brian E. Moroz**
Division of Cancer Epidemiology and Genetics, National Cancer Institute, National Institute of Health, Bethesda, MD

Abstract

We developed models of lymphatic nodes for 6 pediatric and 2 adult hybrid computational phantoms to calculate the lymphatic node dose estimates from external and internal radiation exposures. We derived the number of lymphatic nodes from the recommendations in International Commission on Radiological Protection (ICRP) Publications 23 and 89 at 16 cluster locations for the lymphatic nodes: extrathoracic, cervical, thoracic (upper and lower), breast (left and right), mesentery (left and right), axillary (left and right), cubital (left and right), inguinal (left and right), and popliteal (left and right), for different ages (newborn, 1-, 5-, 10-, 15-year-old, and adult). We modeled each lymphatic node within the voxel format of the hybrid phantoms by assuming that all nodes have identical size derived from published data except narrow cluster sites. The lymph nodes were generated by the following algorithm: (1) selection of the lymph node site among the 16 cluster sites; (2) random sampling of the location of the lymph node within a spherical space centered at the chosen cluster site; (3) creation of the sphere or ovoid of tissue representing the node based on lymphatic node characteristics defined in ICRP Publications 23 and 89. We created lymph nodes until the pre-defined number of lymphatic nodes at the selected cluster site was reached. This algorithm was applied to pediatric (newborn, 1-, 5-, and 10-year-old male, and 15-year-old males) and adult male and female ICRP-compliant hybrid phantoms after voxelization. To assess the performance of our models for internal dosimetry, we calculated dose conversion coefficients, called S values, for selected organs and tissues with Iodine-131 distributed in 6 lymphatic node cluster sites using MCNPX2.6, a well validated Monte Carlo radiation transport code. Our analysis of the calculations indicates that the S values were significantly affected by the location of the lymph node clusters and that the values increased for smaller phantoms due to the shorter inter-organ distances compared to the bigger phantoms. By testing sensitivity of S values to random sampling and voxel resolution, we confirmed that the lymph node model is reasonably stable and consistent for different random samplings and voxel resolutions.

Keywords

lymphatic node; computational hybrid phantom; Monte Carlo transport; S value

1. INTRODUCTION

Organ and tissue absorbed dose in internal dosimetry has been generally evaluated by simulating radiation exposure in computational human phantoms representing reference individuals recommended by International Commission on Radiological Protection (ICRP) (ICRP 1975; ICRP 2002). The capability to realistically model organs and tissues greatly

FOR REPRINTS AND CORRESPONDENCE CONTACT: Choonsik Lee, PhD, Investigator, Radiation Epidemiology Branch, Division of Cancer Epidemiology and Genetics, National Cancer Institute, National Institute of Health, Bethesda, MD 20852, Phone: (301)-443-8224 Fax: (301)-402-0207 leechoonsik@mail.nih.gov.

depends on the type of phantom and the modeling techniques used. Computational phantoms have evolved from the first-generation stylized (or mathematical) phantoms (Cristy and Eckerman 1987; Han *et al* 2006) and the second-generation voxel (or tomographic) phantoms (Caon 2004; ICRP 2009; Zaidi and Xu 2007), to more recently the third-generation hybrid (or NURBS/Polygon Mesh) phantoms (Cassola *et al* 2010; Lee *et al* 2007; Lee *et al* 2010; Segars *et al* 2010; Xu *et al* 2007; Zhang *et al* 2009). The best features of the previous two classes of stylized and voxel phantoms are incorporated into the hybrid phantoms: flexibility and realism, respectively.

Lymphatic tissue consists of reticular fibres and cells, along with lymphocytes distributed throughout whole body. Except the lymphocytes, lymphatic tissues are localized to the active bone marrow and the lymphatic organs: lymph nodes, spleen, thymus, mucous membranes, tonsils, adenoids, Peyer's patches, and the vermiform appendix. The lymphatic nodes, one of the lymphatic organs, are considered by the ICRP to be a radiosensitive target tissue (part of the remainder organs) since ICRP Publication 103 (ICRP 2007). According to the report, there are about 600–700 lymphatic nodes in the adult total body. It is difficult to model the lymph nodes in computational human phantoms because of their complex anatomical distribution.

It was impossible to model the complex structure of the lymphatic nodes within stylized phantoms by using mathematical surface equations. After the introduction of voxel phantoms, investigators began attempting to model the lymphatic nodes. Kramer et al. (Kramer *et al* 2006) manually inserted lymphatic node voxels into their voxel phantoms MAX06 and FAX06 in regions of the armpits, groin, behind the knees, in front of the elbows, the neck, and around abdominal soft-tissue organs. More recently, Zankl et al. (ICRP 2009) reported ICRP reference male and female voxel phantoms with lymphatic nodes. Since the lymph nodes are not identifiable on the computed tomography (CT) images, the tissues were manually drawn at locations specified in anatomical textbooks. The higher distribution at specific locations (e.g., groins, axillae, the hollows of the knees, crooks of the arms) in the textbooks is correctly incorporated. Six different lymphatic node regions are modeled: extrathoracic airways, thoracic airways, head, trunk, arms, and legs. However, they do not attempt to incorporate site-specific number of the lymphatic nodes.

We previously reported the development of an algorithm to model the lymphatic nodes in the adult male hybrid phantom (Lee *et al* 2009). In the current study, we improved the algorithm by accounting for the numbers of the lymphatic nodes and extended it to the pediatric hybrid phantoms. To assess the performance of our models for internal dosimetry, we calculated the dose conversion coefficients, called S values, for selected organs/tissues and the 16 lymphatic node sites considering an iodine-131 (I-131) source distributed in selected lymphatic nodes.

2. MATERIALS AND METHODS

2.1. Hybrid phantom series

We used 8 ICRP-compliant pediatric and adult hybrid phantoms : newborn, 1-year, 5-year, 10-year male, and 15-year-old and adult male and female phantoms developed at the University of Florida and the National Cancer Institute (Lee *et al* 2007; Lee *et al* 2010; Lee *et al* 2008). The phantoms were originally segmented from head and torso CT images of real patients at the given ages. Arms and legs were separately segmented from high resolution CT images of arms and legs of the 18-year-old male, and then scaled to match the standard anthropometric data at each respective age. Four international reference datasets were incorporated into the final phantom series: (1) reference masses of organs and tissues (ICRP 2002), (2) reference elemental compositions of organs and tissues, (3) reference

anthropometric data of the United States (http://www.cdc.gov/nchs/nhanes.htm), and (4) reference dimensions of the alimentary tracts. Each hybrid phantom includes more than 40 organs/tissues as well as 35 detailed skeletal sites. The skeleton is composed of cortical and spongiosa structures to enable detailed dose calculations for active marrow and bone surface.

Because the male and female pediatric phantoms (newborn to 10-year-old) share the same anatomy except gender-specific organs such as prostate, uterus, testes, and ovaries, we only used the male phantoms for those ages in this study. The 15-year-old and adult male and female phantoms were based on totally independent individuals to accurately model their gender-specific anatomy and unique heights and weights. Therefore, we developed a lymph node model for both male and female phantoms of age 15 and adult.

2.2. Anatomical data of lymphatic node model

We identified 16 lymphatic nodal sites each representing a cluster of lymphatic nodes from the literature (Marieb and Hoehn 2007): extrathoracic, cervical, thoracic (upper and lower), breast (left and right), mesentery (left and right), axillary (left and right), cubital (left and right), inguinal (left and right), and popliteal (left and right). We assumed that the lymphatic nodes were symmetrically distributed in case of left and right-sided sites (e.g., axillary). To realistically model the lymphatic nodes, we used additional data such as the diameter of a single node, the site-specific diameter of a lymph node cluster, as well as the number of lymphatic nodes.

Genereux et al. (Genereux and Howie 1984) measured the size and number of lymphatic nodes in the mediastinal region by using computed tomography (CT) images of 39 patients and by dissection at autopsy in 12 cadavers. Depending on their anatomic site, lymphatic nodal size ranges from 0.1 to 2 cm. The average size in the four different zones around mediastinal region is 1.26 × 0.83 cm. Glazer et al. (Glazer *et al* 1985) measured the number and size of normal mediastinal lymphatic nodes via CT images of 56 normal adult patients. They suggested 1 cm as the upper limit of the short axis for a mediastinal node in the transverse CT image plane. Kiyono et al. (Kiyono *et al* 1988) also measured the number and size of normal lymph nodes for each region of the mediastinum from 40 adult cadavers. They propose a standard for maximum normal short transverse diameters for the mediastinum region ranging from 0.8 – 1.2 cm. Based on the literatures, we subsequently defined a standardized nodal diameter of 1 cm for our model in adult male and female for all lymphatic nodes except extrathoracic and upper/lower thoracic sites. In these locations we used a diameter of 0.6 cm because the spaces of residual soft tissues in the head and thoracic regions were too small to allow the inclusion of individual lymphatic nodes larger than 0.6 cm. Using the diameter of a lymph node for an adult male, we calculated age-dependent nodal diameters using the ratio of the lateral width of the phantoms as a factor of proportionality. Table 1 shows the age-dependent nodal diameters for the hybrid phantoms used in this study.

We measured the diameters of the 16 lymph node cluster sites based on the literature (Marieb and Hoehn 2007) and concluded that the diameters are approximately close to the lateral phantom width divided by a factor of 10 except for the mesentery and inguinal lymph sites; in these cases factors of 5 and 15 were used, respectively. The phantom width was calculated by multiplying the number of voxels between left and right limits of the phantoms by the voxel resolution. By using the width of the age-dependent phantom, the cluster diameters were automatically scaled down to the pediatric phantoms. The resulting cluster diameters are tabulated in Table 1.

We derived the number of lymph nodes at the 16 sites from ICRP Publications. The true number of lymph nodes in the human body is large and is difficult to accurately estimate. The ICRP reports that at least 600–700 lymphatic nodes exist within the adult body, 8–37 in the armpits, at least 50–60 in the lung hilus, and 200–500 in the mesentery area (ICRP 2002). We used the center of these ranges for our model. Hence we modeled 650 lymph nodes in the adult male phantom with 55, 350, and 22 in the thoracic (upper and lower), mesentery (left and right), and axiliary (left and right) lymph node sites, respectively. We then uniformly distributed the remainder of the lymph nodes, which were equal to 223 nodes (650−55−350−22=223) to the other lymph node sites (Table 2). We used the site-specific number of lymph nodes in the adult male phantom to derive the site-specific number of lymph nodes in the other phantoms. ICRP Publication 23 provides age-dependent estimates of the number of mesentery lymphatic nodes (ICRP 1975). We adopted the following numbers after some realistic adjustment: 220 for 0–1 year, 400 for 10 year, and 350 for adult. We calculated the number of lymph nodes in the 5-year male phantom by interpolating the number of nodes present in the 1-year-old and 10-year-old phantoms. We assumed the number of lymph nodes for the 15-year-old male and female, and adult female phantoms to be the same as in the adult male. We used the ratio of the number of the mesentery nodes in the pediatric phantoms to the adult phantoms as a factor of proportionality to calculate the site-specific nodal numbers for the other phantoms (Table 2).

2.3. Algorithm for modeling lymphatic nodes

The hybrid phantom is composed of a combination of Non-Uniform Rational B-Spline (NURBS) and polygon mesh (PM) surfaces. The original NURBS/PM hybrid phantom is converted into voxel format to be coupled with Monte Carlo calculation code through a voxelization process previously described by Lee et al (Lee *et al* 2007). In the current study, we used both NURBS/PM and voxel formats to create the lymphatic node model. The procedure involved two steps: (1) identifying location of 16 central points of the 16 lymphatic cluster sites within the NURBS/PM format, and (2) populating lymphatic nodes within the voxel format using an algorithm.

First, we chose 16 points corresponding to the center of the 16 lymphatic cluster sites in the NURBS/PM-format hybrid phantoms using commercial 3D NURBS modeling software[1]. We manually saved the rectangular coordinates of these 16 points for each phantom in ASCII text file. The 8 hybrid phantoms were voxelized using a resolution adequate enough to accurately model the smallest elements in the anatomy (Table 1).

Second, we extended our previous algorithm that incorporates lymphatic nodes in our adult male phantom (Lee *et al* 2009) to more realistically account for the site-dependent number of lymph nodes. This was done using an in-house MATLAB™ (Mathworks, Natick, MA) code to automate the lymph node generation. The MATLAB code uses the voxel phantom data and the necessary anatomical data, i.e., the center and diameter of the 16 clusters, the diameter of a single lymph node, and the derived site-specific nodal numbers. The code generates the individual lymph nodes in two steps: (1) position sampling and (2) node generation. The code consecutively selects each lymph node site and randomly sampled the position of the individual lymphatic nodes within the spherical location bounded by the diameter of the cluster location. Any location already occupied by other organs or the skeleton, excluding residual soft tissue, and lymph nodes already generated is rejected. If the previous criteria are met, sphere or ovoid of tissue representing individual lymphatic nodes were created at the sampled positions. The shape of a single node depends on whether the voxel resolution of a given phantom is isotropic or not. Sphere is generated for the isotropic

[1]Rhinoceros™ (McNeel North America, Seattle, WA)

voxel resolution (e.g., newborn) and ovoid is for the anisotropic resolution phantoms. The code creates lymph nodes until the predefined number of lymph nodes within a given site is reached. We obtained the volume of the site-specific lymph nodes from the resulting voxel phantoms and calculated the mass of the lymph nodes in each site using the density, 1.03 g/cm^3, of the average soft tissue (ICRU 1992). The second step is summarized in Figure 1.

2.4. Visualization of the lymph node model

Once the lymph node model was completed and merged with the other anatomical data in the hybrid voxel phantom, it was rendered in 3-dimensions using Visualization Toolkit (VTK) (KitWare Inc., Clifton Park, NY) for visual inspection. VTK is well tested software library for the visualization of scientific data. It includes routines for viewing and manipulating visual data based on low level functions defined by the OpenGL library. After modeling of lymphatic nodes in the hybrid phantom, each voxel is given a value (tag number 0 – 255) and stored to disk using one byte (8 bits) of data. Using the proper dimensions, orientation, and resolution information, VTK is able to construct the 3-dimensional reference frame needed to properly view the data. The data can then be visualized in any number of ways. In our case, the data was viewed volumetrically and mapped using the tag numbers associated with each voxel. Through different color transfer functions and opacity functions, we were able to view and inspect the lymph node models and thus the accuracy of the lymph node model at various anatomical levels.

2.5. Illustrative calculation of S values

To assess the performance of our lymph node models for use in internal dosimetry, we calculated the dose conversion coefficients, called S values, for I-131 using 6 selected lymphatic node sites considered as source regions and 30 organs and tissues (including the 16 lymphatic node sites) considered as target regions. Source regions included upper and lower thoracic, left and right mesentery, and left and right axiliary lymph node sites. Target organs other than lymphatic nodes included the brain, salivary glands, thyroid, esophagus, left and right lung, stomach wall, liver, small intestine wall, left and right colon wall, skin, urinary bladder wall, and ovaries/testes. I-131 was assumed to be uniformly distributed in each of the selected lymphatic node source regions.

We directly calculated the S values using Monte Carlo radiation transport techniques. Calculations for photons and electrons were done separately. The simulations provided the energy deposition in each target organ r_T per simulated particle, noted as $E_\gamma(r_T)$ and $E_\beta(r_T)$ (MeV/particle) for photons and electrons, respectively, where $M(r_T)$ is the mass of the target organ. We computed the products of the energy deposition per simulated particle and the particle yield (either photon Y_γ or electron Y_β) per nuclear transformation (MBq-s), which we summed to compute the S value (mGy/MBq-s)) (eq. 1):

$$S(r_T \leftarrow r_S) = 1.602 \times 10^{-10} \frac{1}{M(r_T)} \left[E_\gamma(\gamma_T) Y_\gamma + E_\beta(r_T) Y_\beta \right] \quad (1)$$

where 1.602×10^{-10} is the number of joules per MeV. We previously reported the details of the calculation method (Lamart *et al* 2011).

We used a general purpose Monte Carlo radiation transport code, MCNPX2.6 (Pelowitz 2008) to calculate radiation dose per unit administered activity from photon and electron transport using the I-131 emission spectrum provided from ICRP Publication 107 (ICRP 2008). We voxelized the 6 pediatric and 2 adult hybrid phantoms using the resolution mentioned above (Table 1), and implemented lymph nodes using the MATLAB code. Organ- and tissue-specific density and elemental composition were implemented into the

material card of the MCNPX code. The radioactive source was described as a uniform source of radiation within a given source region, by explicitly specifying the location of each voxel included in the source region within the phantom matrix. The location data of the source voxels were generated from each phantom by using an in-house MATLAB code. We conducted the radiation transport simulations using 5×10^8 particle histories to ensure a relative error of less than 1% for most of the source and target organ combinations.

In order to investigate the dosimetric impact of the changes in the new lymph node model, we compared the S values from the new lymph node model with the values from our old model (Lee *et al* 2009).

2.6. Sensitivity of S values to random sampling and voxel resolution

Sensitivity of S values to (1) the randomness of the lymph node generation and (2) the different voxel resolution was tested.

First, two more lymph node models were consecutively generated within adult male voxel phantom using the algorithm of the lymph node generation but with different seeds for random numbers. Organ and lymph node S values were calculated using the two additional phantoms when I-131 is assumed to be distributed within lower thoracic lymph nodes which are relatively located in the middle of the torso region. Average, standard deviation (SD), and coefficient of variation (COV) were calculated for the three sets of S values including the value already calculated from the original adult male voxel phantom and the new S values calculated from two additional phantoms. Although the site-specific and total numbers of lymph nodes were identical within the three phantoms, the locations of each individual lymph node were different.

Second, the adult male hybrid NURBS phantom was voxelized to generate two more adult male voxel phantoms using different voxel resolutions: $0.1 \times 0.1 \times 0.1$ cm^3 and $0.2 \times 0.2 \times 0.2$ cm^3. Organ and lymph node S values were calculated for the two additional voxel phantoms again when I-131 is assumed to be distributed within lower thoracic lymph nodes. Average, SD, and COV were calculated for the three sets of S values including the values from the original adult male voxel phantom with the voxel resolution of $0.1579 \times 0.1579 \times 0.2207$ cm^3 (Table 1) and the two additional phantoms.

3. RESULTS

3.1. Lymphatic node models

We modeled 16 sites of lymphatic nodes in 8 hybrid phantoms using our algorithm. We visually evaluated and validated our algorithm using the visualization of the distribution of the lymph nodes relative to the anatomical and skeletal structures of the phantoms. Figure 2 shows the frontal views of the original newborn hybrid phantom in NURBS format (left) and the lymphatic node model with skeleton (right). All of organs and tissues are visualized in the left figure to help readers understand the location of internal organs relative to that of the lymph nodes. The lymph node models for other phantoms are shown in Figure 3. The smaller diameter used for the lymph nodes at the extrathoracic and upper/lower thoracic sites resulted in smaller sized lymph nodes as compared to other cluster sites.

The comparison of the lymph node masses across the sites and ages enabled us to quantitatively assess our model (Table 3). The age-dependent lymph nodal mass followed the same trend as the number of nodes defined in Table 2. We also compared the total mass of age-dependent lymph node models with the values derived from ICRP Publications (ICRP 1994; ICRP 2002) which we previously reported (Lee *et al* 2009). ICRP Publication 66 reports the masses of lymph nodes in extrathoracic and thoracic regions to be

approximately 15 g each (ICRP 1994). We assumed that 14 different lymphatic node sites in adult male contain a total lymphatic node mass of 15 g each, considering the left and right mesentery sites as a single nodal region and the upper and lower thoracic sites also as a single nodal region. The total mass in our previous study came from the reference mass of the two lymph sites whereas the total mass in the current study starts from the reference nodal numbers in the three lymph node sites. Although the two approaches completely differ, the resulting total lymph node masses reasonably matched within 7% on average.

The site-specific mass and the percent distribution of our lymph nodes in the adult male phantom are compared with those of the ICRP reference adult male phantom (ICRP 2009) in Table 4. The 16 lymph sites were reorganized to match the ICRP category. The distributions of the lymph nodes in the two phantoms reasonably match for trunk, arms, and legs regions. Trunk and legs regions show very good agreement less than 10%.

3.2. S values for I-131 source

We calculated S values for selected organs and tissues using 6 selected lymph node sites as source regions for the newborn, 1-, 5-, 10-year male phantoms, and 15-year and the adult male and female phantoms.

Figure 4 shows the age-dependent S values (mGy/MBq-s) for selected organs close to the two source regions: (a) upper thoracic and (b) right mesentery lymph sites. To make the graphs more readable, we did not include the values for the 15-year and adult female phantoms. With I-131 distributed in the upper thoracic lymph nodes, the esophagus received the greatest dose per unit of administered activity (Figure 4a). Because the upper thoracic lymph nodes are closely surrounding the esophagus and also are close to the lungs, as compared to other organs, there was more energy deposition in the esophagus and lungs than in organs located further from the source. Because the distance between the source and the target tissues is shorter in smaller phantoms, the S values tended to be greater in smaller phantoms. For example, the S values for the esophagus and right lung in the newborn phantom were 15 and 12 times greater than the values of the adult male phantom, respectively. The influence of the source-to-target distance was also observed when the I-131 was distributed in the right mesentery lymph nodes (Figure 4b). The small intestine wall and right colon wall had relatively greater S values than other organs because the mesentery lymph nodes were distributed close to the small intestine and colon (Figure 2). The right colon had larger S values than the left colon because the source was distributed in the right mesentery lymph nodes. For the newborn phantom, the S value for the right colon wall was twice as large as the value for the left colon wall. The S values did not always increase with decreasing age, e.g., the S values slightly decreased in the 1-year-old and the newborn phantoms as compared to the computed S values observed in the 5-year-old phantom. The inter-organ distance generally increase with growth; however, the spatial distribution of the mesentery nodes relative to the right colon, for example, may be more independent of growth in our models.

We calculated the S values for selected lymph node sites assuming I-131 was distributed in the (a) left axillary and (b) lower thoracic lymph nodes (Figure 5). The S value resulting from self-irradiation for the left axillary nodes was about 30,000 and 10,000 times larger than the upper thoracic nodes in the newborn and adult male, respectively (not shown in Figure 5 to make it more readable). Because of their close proximity to the left axillary lymph nodes, the upper/lower thoracic and left breast lymph nodes had relatively greater S values when compared with other lymph node sites. Upper thoracic lymph nodes had the highest S values when I-131 was distributed in the lower thoracic nodes, and then were followed by the right and left breast lymph nodes (Figure 5b).

3.3. Comparison with the previous adult lymph node model

We compared the S values from the new lymph node model with the values from our old model (Lee *et al* 2009) that we previously reported to investigate the dosimetric impact of the changes in the new lymph node model. In our old model, a total of 278 lymph nodes are placed within the adult male phantom by randomly generating the lymph nodes until matching total lymph node mass to the estimate of 210 g. In the new model, however, we generated 657 lymph nodes (Table 2) to better match the reference nodal numbers, 600–700 reported in the ICRP Publication 89 of which mass is 223 g in total. The new model includes more than twice more lymph nodes as compared to the old model and most of the additional nodes were placed in the mesentery sites to follow the reference range, 200–500 in the ICRP Publication 89. Figure 8 shows the comparison of frontal views of lymph node models with skeleton of the old (left) and new (right) models in the adult male phantoms. The increase of the lymph nodes number and cluster size in the mesentery region is noticeable in the new model.

To investigate the dosimetric impact of the changes made in our new lymph node model, we compared the S values calculated from the new model with the values from the old model that we previously reported (Lee *et al* 2009). Figure 6(a) and 6(b) shows the ratios of organ and lymph node S values, respectively, from the old lymph node model to the values from the new model when I-131 is localized in the right and left mesentery lymph nodes where most significant change was made in the new model. The S values from the new model are overall higher than those from the old one as shown in Figure 6(a). This is attributed to the decreased distance between new mesentery lymph node cluster and the surrounding organs corresponding to the expansion of the mesentery lymph node cluster in the new model. Photons generated in the new mesentery lymph node model experience less attenuation before entering the target organs than those in the old model. The old and new lymph node models were implemented into the identical adult male phantom anatomy which made it easy to evaluate the dosimetric impact of the changes in the lymph node models on organ S values. However, it is difficult to investigate their impact on lymph node S values since the diameter and location of the lymph node clusters were changed in the new model as compared to the old one as shown in Figure 8. Self S values of right and left mesentery lymph nodes from the right and left mesentery sources, respectively, are lower in the new model than the old one as shown in Figure 6(b) because the bigger cluster size in the new model provides more attenuation for the cross-firing photons among the mesentery lymph nodes. The location of the lower thoracic lymph nodes was relocated upward in the new model based on the literature (Marieb and Hoehn 2007) which caused the decrease of the S values for the lower thoracic lymph node target in the new model as compared to the values from the old model.

As compared to mesentery lymph nodes in Figure 6(a) and 6(b), relatively minor changes were made in the new axillary lymph nodes. Figure 7 shows the ratio of organ S values from the old model to the values from the new model when I-131 is localized in the right and left axillary lymph nodes. Difference is observed less than 20% which is smaller than the case of the mesentery lymph nodes. S values for the new axillary lymph nodes are overall greater than the values for the old ones. As shown in Figure 8, less number of lymph nodes is populated in the new model and they are more condensed toward torso region compared to the old model which has some nodes located farther from the torso. Those farther lymph nodes may contribute to the smaller organ S values in the old axillary lymph node model.

3.4. Sensitivity of S values to random sampling and voxel resolution

Table 5 and 6 show the organ and lymph node S values, respectively, for the three adult male (AM) voxel phantoms including the original phantom (AM1) and two additional

phantoms (AM2 and AM3) which were generated in three consecutive trials using the same lymph node generation algorithm but different random number seeds. I-131 was assumed to be distributed within lower thoracic lymph nodes. Average, SD, and COV (%) are also included in both tables. Although the locations of individual lymph node were randomly sampled among the three voxel phantoms, COV of organ S values was less than 10% as shown in Table 5. COV of lymph node S values (Table 6) was also less than 10% for most of lymph node sites except right and left popliteal sites. The COV higher than 10% in the popliteal lymph nodes is attributed to the poor statistics in Monte Carlo calculations. Percent relative errors from Monte Carlo calculation are also included next to the S values in Table 6 for reference. It was impossible to reduce the relative errors of the popliteal S values down to less than 1% even using the 5×10^8 photon history because the lymph site is too far from the source region as compared to other lymph sites as shown in Figure 8. Table 6 is sorted in ascending order of S values to highlight the magnitude of S values. The S value for the left popliteal lymph nodes, 5.5×10^{-11} mGy/MBq-s, is 10,000 times smaller than the value for the right breast lymph node, 5.6×10^{-7} mGy/MBq-s.

The organ and lymph node S values from another set of the three voxel phantoms are tabulated in Table 7 and 8, respectively, including the values from the original adult male voxel phantom with the voxel resolution of $0.1579 \times 0.1579 \times 0.2207$ cm^3 (0.0055 cm^3) and the two additional voxel phantoms, AM4 and AM5, with the voxel resolution of $0.1 \times 0.1 \times 0.1$ cm^3 (0.0010 cm^3) and $0.2 \times 0.2 \times 0.2$ cm^3 (0.0080 cm^3), respectively. I-131 was assumed to be distributed within lower thoracic lymph nodes. Similar with the sensitivity to random samplings (Table 5), organ S values from the three voxel phantoms with different voxel resolutions match well within the COV of 10%. As shown in Table 6, COV for lymph node S values is less than 10% except for the popliteal lymph nodes which show the COV way greater than 10%. Again the magnitude of Monte Carlo relative errors for those S values is greater than 20% which means the results are unreliable. Again the popliteal lymph node S values are much smaller than the values for other lymph nodes.

Based on the two different types of sensitivity analysis, we conclude that the lymph node model is reasonably stable and consistent for different random samplings and voxel resolutions.

4. DISCUSSION

To provide an anatomically accurate model of the lymph nodes across ages and genders for radiation dosimetry, we developed an algorithm to automatically incorporate lymphatic nodes within computational human phantoms based on available reference data. We generated lymph node models for 8 hybrid phantoms, i.e., newborn, 1-, 5-, 10-year male phantoms, and 15-year and adult male and female phantoms using the algorithm. The 16 site-specific numbers of lymph nodes well matched the reference numbers reported by ICRP Publications. The resulting total lymph node mass also reasonably matched the reference lymph node mass derived from ICRP Publications. To further evaluate our lymph node model, we calculated internal dose conversion factors (S values) using a radiation transport code that employs Monte Carlo radiation transport techniques. As expected, the source-to-target distance drove the magnitude of the S values, which generally decreased with phantom size, because of increasing distance between the lymph node sources and the target organs or tissue. Our work provides an anatomically improved model of lymph nodes for radiation dosimetry when compared with the previous methods of modeling where lymph nodes are manually drawn within the voxel phantoms by referring to anatomy textbooks (ICRP 2009) or manually segmented from medical images with limited visibility of lymph nodes (Kramer *et al* 2006). We checked the dosimetric impact of the better realism in our new model by comparing the S values with those from our old lymph node model.

The location of each lymph node was randomly sampled and fixed once the modeling is done within a given voxel phantom. The spatial distribution of lymph nodes would be different every time we apply the algorithm. However, the lymph nodes are generated within tight constraints such as pre-defined cluster radius and the resulting lymph node model will not provide a significant dosimetric uncertainty which was confirmed by the sensitivity analysis of random sampling. Minor dose uncertainty caused by the variation of exact size, shape, and location of lymph nodes might be at the similar level of uncertainty attributed to an individual variability. Other organ and tissue models than lymph nodes within most of voxel phantoms are also having the issue of individual variability (e.g., shape and location of stomach). Other existing lymph node models developed through manual drawings or segmentations also might involve the similar level of dose uncertainty.

The size of individual lymph node was determined by the breadth of our reference pediatric and adult phantoms which follow the standard anthropometric data. If one intends to use our lymph node model for a voxel phantom with non-50^{th} percentile body size, we would recommend using the lymph node size tabulated in Table 1 corresponding to the age of the voxel phantom instead of its breadth since the nodal size may rather depend on age than body size.

Our lymph node model still may be improved by further investigations. We used the available published data on lymph nodes location and size and made assumptions to build our model, e.g., we derived the site-specific number of lymph nodes for smaller phantoms using the ratio of mesentery lymph nodes. To further validate the assumption, it may be necessary to use high-resolution CT images for each lymph node site and across the specific ages and both genders. This task may be challenging because lymph nodes are difficult to identify in CT images. Also, whole body scans are less frequent than CT scans covering a limited section of the body. One could derive the relative number of lymph nodes among different sites using partial body scans from different patients, but then inter-individual variability needs to be considered.

5. CONCLUSION

In this study we proposed a more anatomically accurate (compared to previous models) lymph node model for 6 pediatric and 2 adult male and female phantoms. Our model compared well with anatomical reference data from ICRP and yielded favorable results for most target organs and tissues when computing S values, which are especially sensitive to inter-organ distances. The pediatric hybrid phantoms, with the incorporated lymphatic node models, will be used to derive reference radiation dose estimates for radiation protection purpose.

References

Caon M. Voxel-based computational models of real human anatomy: a review. Radiation and Environmental Biophysics. 2004; 42(4):229–235. [PubMed: 14730450]

Cassola V, de Melo Lima V, Kramer R, Khoury H. FASH and MASH: female and male adult human phantoms based on polygon mesh surfaces: I. Development of the anatomy. Physics in Medicine and Biology. 2010; 55:133–162. [PubMed: 20009183]

Cristy, M.; Eckerman, KF. Specific absorbed fractions of energy at various ages from internal photon sources. Vol. 1–7. Oak Ridge, TN: Oak Ridge National Laboratory; 1987. ORNL/TM-8381

Genereux G, Howie J. Normal mediastinal lymph node size and number: CT and anatomic study. American Journal of Roentgenology. 1984; 142(6):1095–1100. [PubMed: 6609588]

Glazer G, Gross B, Quint L, Francis I, Bookstein F, Orringer M. Normal mediastinal lymph nodes: number and size according to American Thoracic Society mapping. American Journal of Roentgenology. 1985; 144(2):261–265. [PubMed: 3871268]

Han EY, Bolch W, Eckerman K. Revisions to the ORNL series of adult and pediatric computational phantoms for use with the MIRD schema. Health Physics. 2006; 90(4):337–356. [PubMed: 16538139]

ICRP. Report on the Task Group on Reference Man. Oxford, UK: International Commission on Radiological Protection; 1975. ICRP Publication 23

ICRP. Human respiratory tract model for radiological protection : a report of a Task Group of the International Commission on Radiological Protection. Oxford: International Commission on Radiological Protection; 1994. p. xiip. 482ICRP publication 66

ICRP. Ann ICRP. 2002. Basic anatomical and physiological data for use in radiological protection : reference values; p. xip. 265ICRP publication 89

ICRP. The 2007 Recommendations of the International Commission on Radiological Protection. Ann ICRP. 2007; 37(2–4) ICRP publication 103.

ICRP. Nuclear Decay Data for Dosimetric Calculations. Ann ICRp. 2008; 8(3) ICRP publication 107.

ICRP. Adult Reference Computational Phantoms. Ann ICRP. 2009; 39(2) ICRP Publication 110.

ICRU. International Commission on Radiation Units and Measurements. 1992. Proton and Neutron Interaction Data for Body Tissues. ICRU report 46

Kiyono K, Sone S, Sakai F, Imai Y, Watanabe T, Izuno I, Oguchi M, Kawai T, Shigematsu H, Watanabe M. The number and size of normal mediastinal lymph nodes: a postmortem study. American Journal of Roentgenology. 1988; 150(4):771–776. [PubMed: 3258087]

Kramer R, Khoury HJ, Vieira JW, Lima VJ. MAX06 and FAX06: update of two adult human phantoms for radiation protection dosimetry. Physics in Medicine and Biology. 2006; 51(14): 3331–46. [PubMed: 16825733]

Lamart S, Bouville A, Simon SL, Eckerman KF, Melo D, Lee C. Comparison of internal dosimetry factors for three classes of adult computational phantoms with emphasis on I-131 in the thyroid. Physics in Medicine and Biology. 2011; 56:7317. [PubMed: 22040775]

Lee C, Kaufman K, Pafundi D, Bolch W. An Algorithm for Lymphatic Node Placement in Hybrid Computational Phantoms—Applications to Radionuclide Therapy Dosimetry. IEEE Transactions. 2009; 97(12):2098–2108.

Lee C, Lee C, Lodwick D, Bolch WE. Development of hybrid computational phantoms of newborn male and female for dosimetry calculation. Physics in Medicine and Biology. 2007; 52:3309–3333. [PubMed: 17664546]

Lee C, Lodwick D, Hurtado J, Pafundi D, Williams JL, Bolch WE. The UF family of reference hybrid phantoms for computational radiation dosimetry. Physics in Medicine and Biology. 2010; 55(2): 339–63. [PubMed: 20019401]

Lee C, Lodwick D, Williams JL, Bolch WE. Hybrid computational phantoms of the 15-year male and female adolescent: applications to CT organ dosimetry for patients of variable morphometry. Medical Physics. 2008; 35(6):2366–2382. [PubMed: 18649470]

Marieb, EN.; Hoehn, K. Human anatomy & physiology. Pearson Education; 2007.

Pelowitz, DB. MCNPX user's manual Version 2.6.0. Los Alamos National Laboratory; 2008. LA-CP-05-0369

Segars W, Sturgeon G, Mendonca S, Grimes J, Tsui B. 4D XCAT phantom for multimodality imaging research. Medical Physics. 2010; 37:4902. [PubMed: 20964209]

Xu XG, Taranenko V, Zhang J, Shi C. A boundary-representation method for designing whole-body radiation dosimetry models: pregnant females at the ends of three gestational periods--RPI-P3, -P6 and -P9. Physics in Medicine and Biology. 2007; 52(23):7023–44. [PubMed: 18029991]

Zaidi H, Xu XG. Computational anthropomorphic models of the human anatomy: The path to realistic Monte Carlo modeling in radiological sciences. Annual Review of Biomedical Engineering. 2007; 9:471–500.

Zhang J, Na Y, Caracappa P, Xu X. RPI-AM and RPI-AF, a pair of mesh-based, size-adjustable adult male and female computational phantoms using ICRP-89 parameters and their calculations for organ doses from monoenergetic photon beams. Physics in Medicine and Biology. 2009; 54:5885. [PubMed: 19759412]

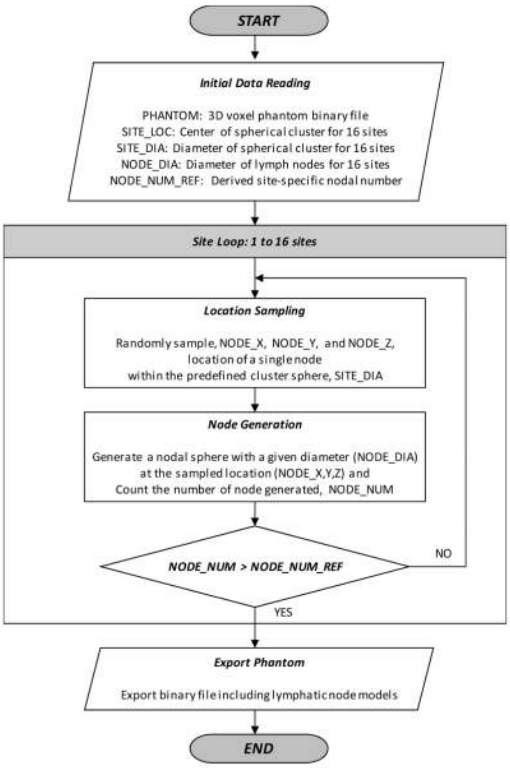

Figure 1.
Flowchart describing the algorithm to insert the lymph nodes in voxel phantoms.

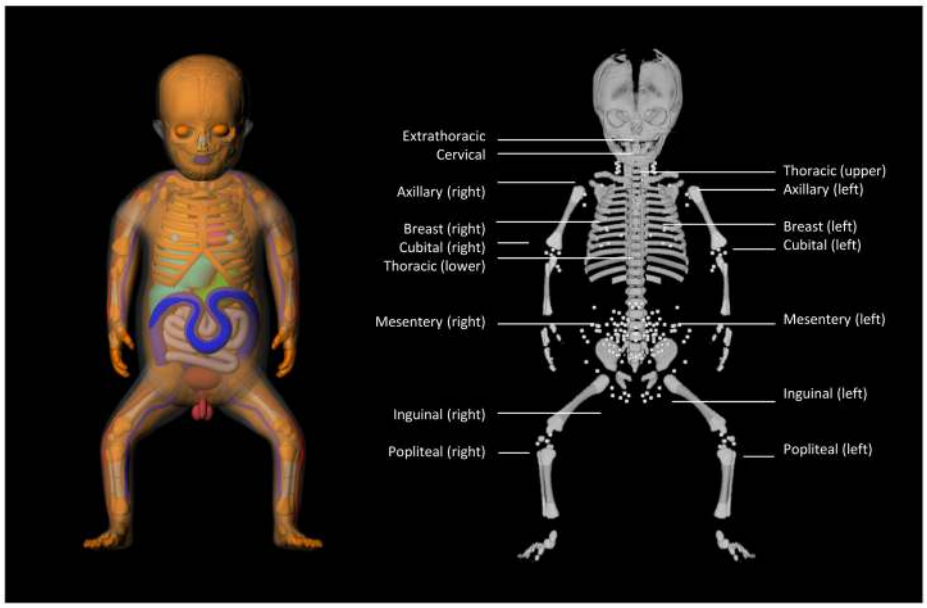

Figure 2.
3D rendering of the skeleton of the newborn phantom and the incorporated lymph nodes.

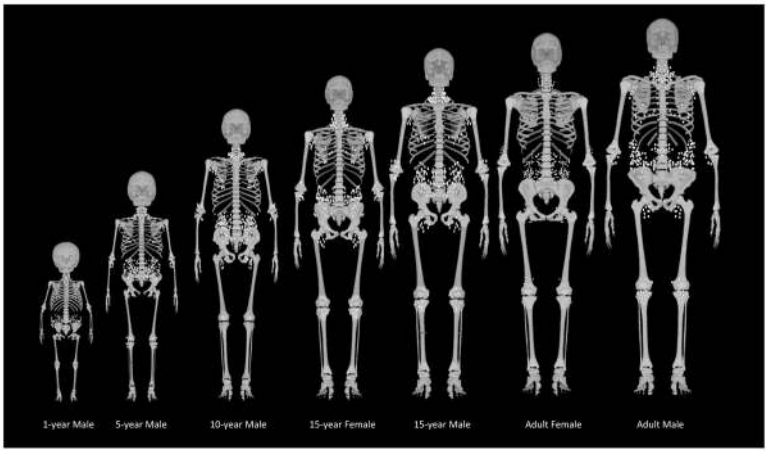

Figure 3.
3D rendering of the skeleton and lymph nodes of the 1-, 5-, 10-, 15-year and adult male phantoms.

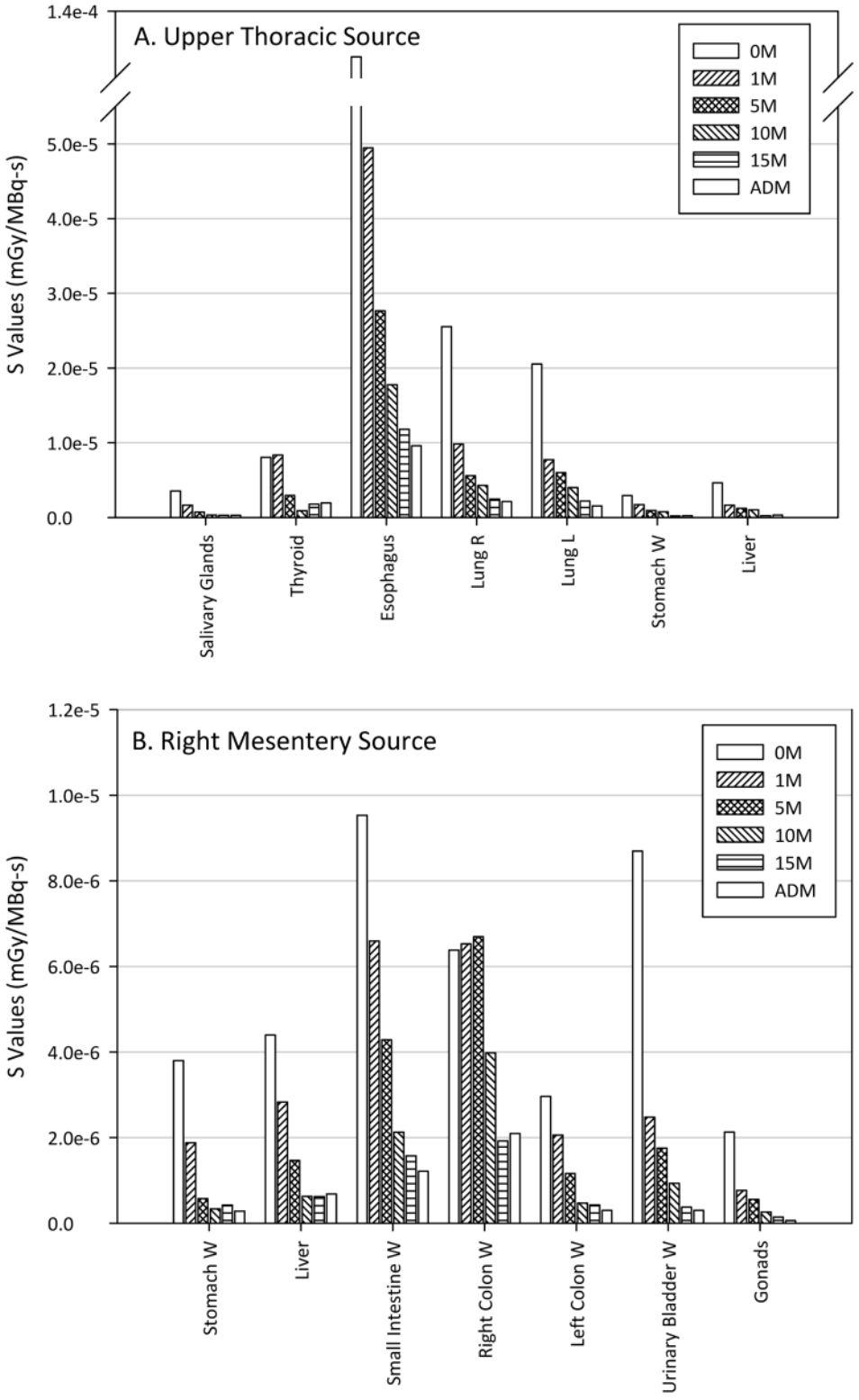

Figure 4.
S values (mGy/MBq-s) for selected organs with I-131 distributed in (a) the upper thoracic lymph site and (b) the right mesentery lymph site.

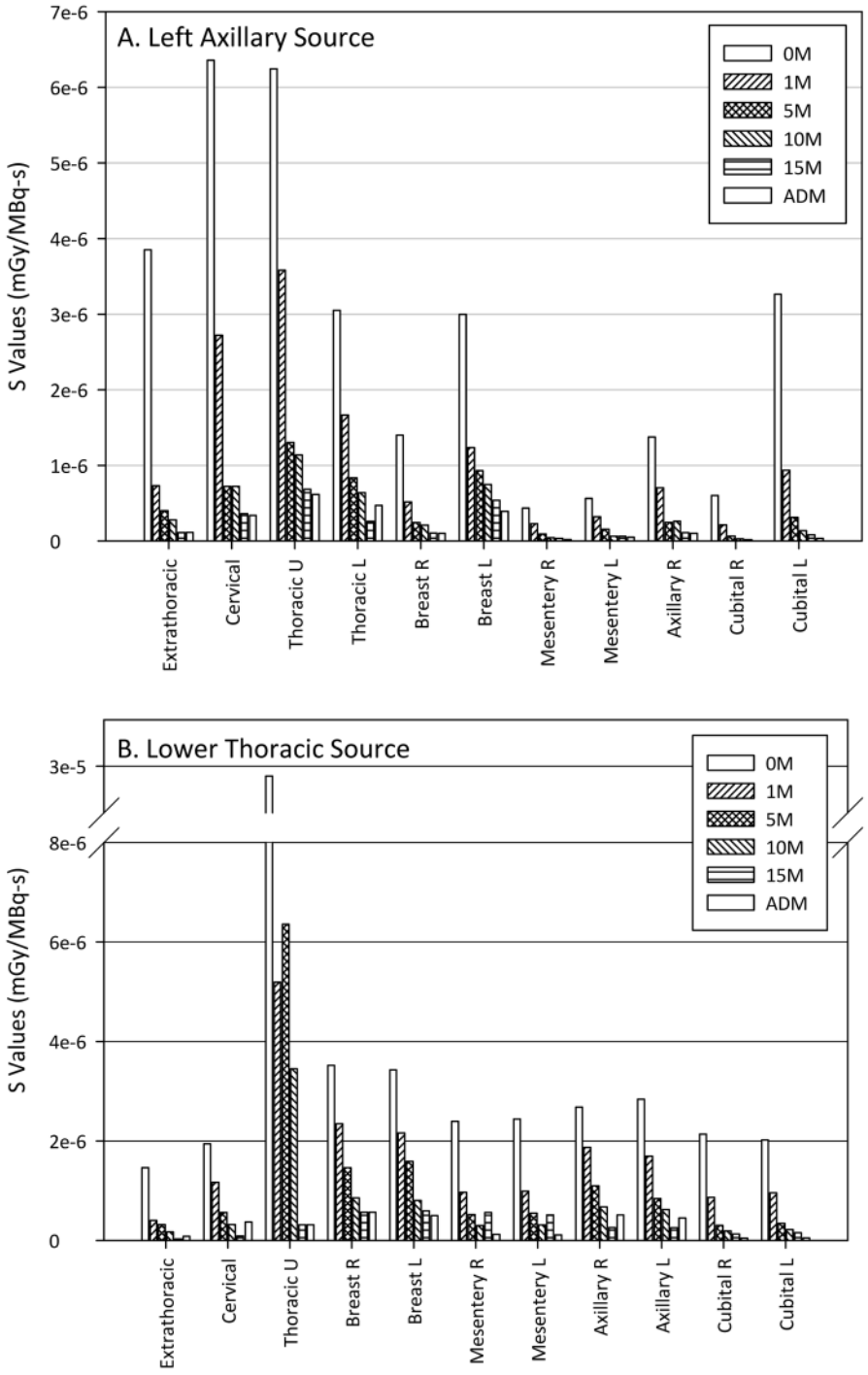

Figure 5.
S values (mGy/MBq-s) for selected lymph node sites with I-131 distributed in (a) the left axillary lymph site and (b) the lower thoracic lymph site.

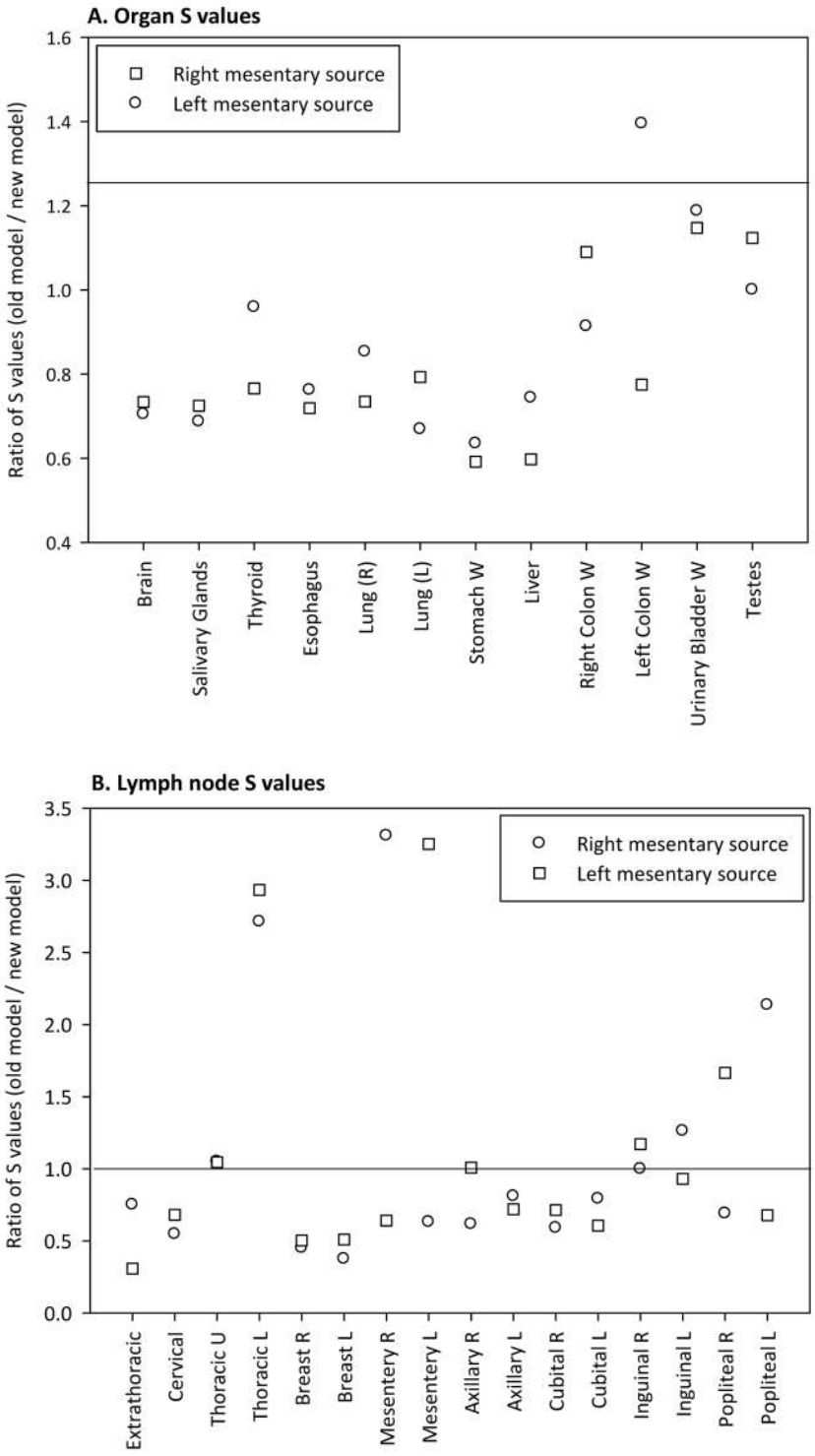

Figure 6.

Ratio of the (a) organ and (b) lymph node S values from the old lymph node model previously reported to the values from the new model developed in the current study when I-131 is localized in the right and left mesentery lymph nodes.

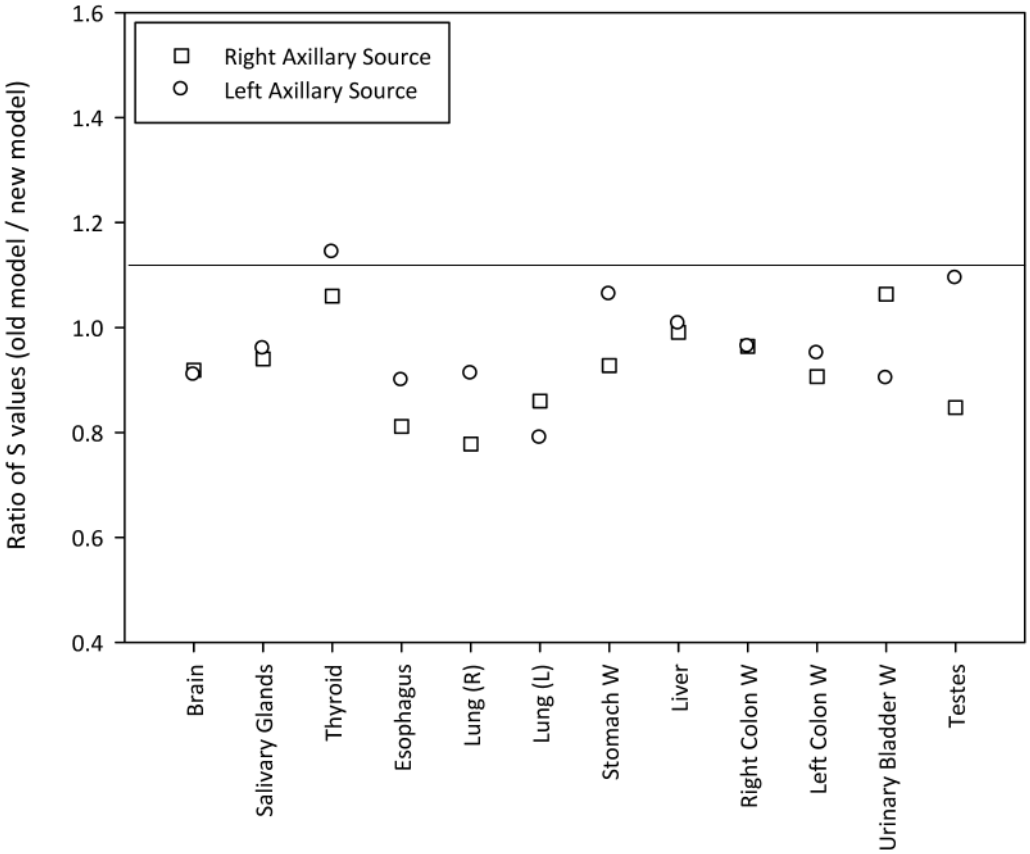

Figure 7.
Ratio of the organ S values from the old lymph node model to the values previously reported from the new model developed in the current study when I-131 is localized in the right and left axillary lymph nodes.

Figure 8.
Comparison of the frontal views of the old (left) and new (right) lymph node models with the skeleton in the adult male hybrid voxel phantom.

Table 1

Anatomical parameters used in the development of the lymph node model: voxel resolution of the 8 hybrid phantoms, the width of the phantoms, the diameter of a single lymph node, and the radius of a lymph cluster site.

Anatomical Parameters	0 Male	1 Male	5 Male	10 Male	15 Female	15 Male	Adult Female	Adult Male
Voxel Resolution (cm)								
X-axis7	0.0663	0.0663	0.0850	0.0990	0.1200	0.1250	0.1260	0.1579
Y-axis	0.0663	0.0663	0.0850	0.0990	0.1200	0.1250	0.1260	0.1579
Z-axis	0.0663	0.1400	0.1928	0.2425	0.2828	0.2832	0.2700	0.2207
Phantom Width (cm)	23.2	26.3	36.0	42.8	49.0	52.0	49.1	57.5
Nodal Diameter (cm)								
Normal sites	0.4	0.5	0.6	0.7	0.9	0.9	0.9	1.0
Narrow sites[1]	0.2	0.3	0.4	0.4	0.5	0.5	0.5	0.6
Site Radius (cm)								
Normal sites (phantom width/10)	2.3	2.6	3.6	4.3	4.9	5.2	4.9	5.7
Mesentery site (phantom width/5)	4.6	5.3	7.2	8.6	9.8	10.4	9.8	11.5
Inguinal site (phantom width/15)	1.5	1.8	2.4	2.9	3.3	3.5	3.3	3.8

[1] Narrow sites include extrathoracic, upper thoracic, and lower thoracic sites.

Table 2

Number of lymph nodes to be modeled at 16 sites for 8 hybrid phantoms. We derived the site-specific number of lymph nodes for the adult male from ICRP Publications (ICRP 1975; ICRP 2002) and we calculated the values for other phantoms using the ratio of the number of mesentery lymph nodes. The ICRP reference nodal numbers is included in the last column. The numbers obtained from ICRP Publications are indicated in italic and bold.

Lymphatic nodal site	0M	1M	5M	10M	15F	15M	ADF	ADM	Reference nodal numbers for adult
Extrathoracic	14	14	24	26	23	23	23	23	
Cervical	14	14	24	26	23	23	23	23	
Thoracic (upper and lower)	35	35	57	63	55	55	55	***55***	50–60
Breast (left and right)	29	29	47	53	46	46	46	46	
Mesentery (left and right)	***220***	***220***	360	***400***	350	350	***350***	***350***	200–500
Axiliary (left and right)	14	14	23	25	22	22	22	***22***	8–37
Cubital (left and right)	29	29	47	53	46	46	46	46	
Inguinal (left and right)	29	29	47	53	46	46	46	46	
Popliteal (left and right)	29	29	47	53	46	46	46	46	
Total	413	413	676	751	657	657	657	657	600–700
Ratio of pediatric mesentery nodal numbers to adult	0.63	0.63	1.03	1.14	1.00	1.00	1.00	1.00	

Phys Med Biol. Author manuscript; available in PMC 2014 January 02.

Table 3

Mass of the lymph nodes at 16 sites for 8 hybrid phantoms. We compared the total mass of the lymph nodes for each phantom with the values derived from ICRP Publications 66 and 89.

Lymphatic nodal site	0M	1M	5M	10M	15F	15M	ADF	ADM
Extrathoracic	0.06	0.11	0.47	0.83	1.30	1.36	1.35	1.67
Cervical	1.00	2.08	7.96	15.20	23.04	25.04	23.96	30.08
Thoracic U[1]	0.05	0.12	0.47	0.83	1.30	1.41	1.38	1.73
Thoracic L	0.08	0.16	0.56	1.13	1.61	1.73	1.68	2.23
Breast R	0.18	0.38	1.37	2.63	4.01	4.35	4.22	5.41
Breast L	0.18	0.38	1.37	2.63	4.01	4.35	4.22	5.41
Mesentery R	1.86	4.15	15.42	29.23	44.08	47.89	45.87	59.56
Mesentery L	1.96	4.16	15.42	29.23	44.08	47.89	45.87	59.56
Axiliary R	0.14	0.30	1.03	2.05	3.01	3.27	3.16	4.06
Axiliary L	0.14	0.30	1.03	2.05	3.01	3.27	3.16	4.06
Cubital R	0.25	0.53	2.06	3.80	6.01	6.53	6.33	8.12
Cubital L	0.25	0.53	2.06	3.80	6.01	6.53	6.33	8.12
Inguinal R	0.25	0.53	2.06	3.80	6.01	6.53	6.33	8.12
Inguinal L	0.25	0.53	2.06	3.80	6.01	6.53	6.33	8.12
Popliteal R	0.25	0.53	2.06	3.80	6.01	6.53	6.33	8.12
Popliteal L	0.25	0.53	2.06	3.80	6.01	6.53	6.33	8.12
Total mass (g)								
Developed in this study	7	15	57	112	115	180	173	223
Derived from ICRP Publications	10	29	55	92	152	161	173	210
Percent difference (%)	29	47	−5	−21	25	−12	0	−6

[1] Lymph node sites in bold letters were used for source tissues in the illustrative S value calculations.

Phys Med Biol. Author manuscript; available in PMC 2014 January 02.

Table 4

Comparison of mass and distribution of the lymph node models between ICRP and hybrid adult male phantoms. The lymph sites in the hybrid phantom were reorganized to match the ICRP category.

ICRP Reference Adult Male Phantom			*Hybrid Adult Male Phantom*			Ratio of distribution (Hybrid/ICRP)
Lymph node sites	**Mass (g)**	**Distribution (%)**	**Lymph node sites**	**Mass (g)**	**Distribution (%)**	
ET airways	2.3	1.6	Extrathoracic	1.7	0.8	0.46
Thoracic airways	6.4	4.6	Thoracic upper and lower	4.0	1.8	0.38
Head	6.0	4.3	Cervical	30.1	13.5	3.12
Trunk	104.4	75.7	Axillary RL, breast RL, mesentery RL, inguinal RL	154.3	69.4	0.92
Arms	7.8	5.7	Cubital RL	16.2	7.3	1.29
Legs	11.1	8.0	Popliteal RL	16.2	7.3	0.91
Total	138.0			222.5		1.61

Table 5

Organ S values (mGy/MBq-s) for three adult male voxel phantoms: original one (AM1) and two more adult male phantoms (AM2 and AM3) where lymph nodes were randomly generated in two consecutive trials when I-131 is distributed within lower thoracic lymph nodes. Average, Standard Deviation (SD) and coefficient of variation (COV) are included.

Organs	AM1 1st trial	AM2 2nd trial	AM3 3rd trial	Average	SD	COV
Brain	2.5E-08	2.5E-08	2.6E-08	2.5E-08	6.6E-10	2.6%
Salivary Glands	8.5E-08	8.6E-08	9.1E-08	8.8E-08	3.4E-09	3.9%
Thyroid	3.1E-07	3.0E-07	3.2E-07	3.1E-07	1.1E-08	3.7%
Esophagus	9.7E-06	9.7E-06	1.1E-05	1.0E-05	5.6E-07	5.6%
Lung (R)	2.0E-06	2.0E-06	2.0E-06	2.0E-06	3.1E-08	1.6%
Lung (L)	1.3E-06	1.3E-06	1.3E-06	1.3E-06	1.5E-09	0.1%
Stomach W	8.2E-07	8.2E-07	7.5E-07	7.9E-07	4.3E-08	5.4%
Liver	1.1E-06	1.1E-06	1.0E-06	1.1E-06	6.7E-08	6.1%
Small Intestine Wall	1.2E-07	1.2E-07	1.0E-07	1.1E-07	6.3E-09	5.7%
Right Colon W	9.9E-08	1.0E-07	9.3E-08	9.7E-08	4.1E-09	4.2%
Left Colon W	1.3E-07	1.4E-07	1.2E-07	1.3E-07	6.3E-09	4.8%
Skin	9.0E-08	9.0E-08	8.9E-08	9.0E-08	4.9E-10	0.5%
Urinary Bladder W	2.1E-08	1.9E-08	1.7E-08	1.9E-08	1.7E-09	9.1%
Gonads	4.1E-09	4.3E-09	3.9E-09	4.1E-09	1.8E-10	4.5%

Table 6

Lymph node

S values (mGy/MBq-s) for three adult male voxel phantoms: original one (AM1) and two more adult male phantoms (AM2 and AM3) where lymph nodes were randomly generated in two consecutive trials when I-131 is distributed within lower thoracic lymph nodes. Relative error (%) from Monte Carlo calculation was included for each S value. Average, Standard Deviation (SD) and coefficient of variation (COV) of the three S values from the three phantoms are included.

Lymph Site	AM1 1st trial	RE(%)	AM2 2nd trial	RE(%)	AM3 3rd trial	RE(%)	Average	SD	COV
Lymph-Popliteal L	5.5E-11	18.9%	1.5E-10	18.7%	1.3E-10	19.4%	1.1E-10	5.2E-11	45.8%
Lymph-Popliteal R	3.1E-10	15.9%	1.3E-10	19.2%	1.4E-10	13.7%	1.9E-10	1.0E-10	51.7%
Lymph-Inguinal R	4.7E-09	2.7%	5.0E-09	2.7%	4.7E-09	2.9%	4.8E-09	1.7E-10	3.4%
Lymph-Inguinal L	4.8E-09	2.8%	5.0E-09	2.6%	4.8E-09	2.9%	4.9E-09	9.8E-11	2.0%
Lymph-Cubital R	4.7E-08	0.9%	5.2E-08	1.0%	5.5E-08	0.9%	5.1E-08	3.8E-09	7.5%
Lymph-Cubital L	5.3E-08	0.9%	5.3E-08	0.9%	5.4E-08	0.9%	5.3E-08	8.2E-10	1.5%
Lymph-Extrathoracic	8.1E-08	1.5%	9.1E-08	1.5%	9.0E-08	1.5%	8.7E-08	5.6E-09	6.4%
Lymph-Mesentery L	1.1E-07	0.2%	1.1E-07	0.2%	1.1E-07	0.2%	1.1E-07	8.4E-10	0.7%
Lymph-Mesentery R	1.2E-07	0.2%	1.2E-07	0.2%	1.1E-07	0.2%	1.2E-07	3.8E-09	3.3%
Lymph-Cervical	3.7E-07	0.2%	3.7E-07	0.2%	4.0E-07	0.2%	3.8E-07	1.6E-08	4.1%
Lymph-Axillary L	4.5E-07	0.4%	4.6E-07	0.5%	4.7E-07	0.4%	4.6E-07	9.6E-09	2.1%
Lymph-Breast L	5.0E-07	0.4%	5.0E-07	0.4%	5.9E-07	0.4%	5.3E-07	5.2E-08	9.8%
Lymph-Axillary R	5.2E-07	0.4%	5.3E-07	0.4%	5.5E-07	0.4%	5.3E-07	1.6E-08	3.1%
Lymph-Breast R	5.7E-07	0.4%	5.7E-07	0.4%	6.6E-07	0.3%	6.0E-07	5.5E-08	9.2%
Lymph-Thoracic U	8.1E-06	0.2%	8.1E-06	0.2%	8.9E-06	0.2%	8.4E-06	4.7E-07	5.6%
Lymph-Thoracic L	1.2E-02	0.0%	1.2E-02	0.0%	1.2E-02	0.0%	1.2E-02	2.4E-04	2.0%

Table 7

Organ S values (mGy/MBq-s) for three adult male voxel phantoms: the original one (AM1) and two more adult male phantoms (AM4 and AM5) with different voxel resolutions, 0.0055, 0.0010, and 0.0080 cm^3, respectively, when I-131 is distributed within lower thoracic lymph nodes. Average, Standard Deviation (SD) and coefficient of variation (COV) are included.

Organs	AM1 0.0055 cm^3	AM4 0.0010 cm^3	AM5 0.0080 cm^3	Average	SD	COV
Brain	2.5E-08	2.4E-08	2.6E-08	2.5E-08	8.7E-10	3.5%
Salivary Glands	8.5E-08	8.4E-08	9.0E-08	8.6E-08	3.4E-09	4.0%
Thyroid	3.1E-07	2.9E-07	3.1E-07	3.0E-07	9.4E-09	3.1%
Esophagus	9.7E-06	9.5E-06	9.4E-06	9.5E-06	1.5E-07	1.6%
Lung (R)	2.0E-06	2.0E-06	2.1E-06	2.0E-06	5.6E-08	2.8%
Lung (L)	1.3E-06	1.3E-06	1.4E-06	1.3E-06	3.5E-08	2.6%
Stomach W	8.2E-07	8.9E-07	7.5E-07	8.2E-07	6.7E-08	8.2%
Liver	1.1E-06	1.2E-06	1.0E-06	1.1E-06	7.6E-08	6.8%
Small Intestine Wall	1.2E-07	1.3E-07	1.1E-07	1.2E-07	8.8E-09	7.6%
Right Colon W	9.9E-08	1.1E-07	9.5E-08	1.0E-07	6.7E-09	6.6%
Left Colon W	1.3E-07	1.5E-07	1.3E-07	1.4E-07	1.1E-08	7.9%
Skin	9.0E-08	8.8E-08	9.0E-08	9.0E-08	1.2E-09	1.4%
Urinary Bladder W	2.1E-08	2.0E-08	1.8E-08	2.0E-08	1.6E-09	7.9%
Gonads	4.1E-09	4.6E-09	4.0E-09	4.2E-09	3.4E-10	8.0%

Table 8

Lymph node

S values (mGy/MBq-s) for three adult male voxel phantoms: the original one (AM1) and two more adult male phantoms (AM4 and AM5) with different voxel resolutions, 0.0055, 0.0010, and 0.0080 cm^3, respectively, when I-131 is distributed within lower thoracic lymph nodes. Relative error (%) from Monte Carlo calculation was included for each S value. Average, Standard Deviation (SD) and coefficient of variation (COV) of the three S values from the three phantoms are included.

Lymph Site	AM1 0.0055 cm^3	RE(%)	AM4 0.0010 cm^3	RE(%)	AM5 0.0080 cm^3	RE(%)	Average	SD	COV
Lymph-Popliteal L	5.5E-11	24.0%	1.2E-10	17.3%	1.1E-10	27.0%	9.3E-11	3.4E-11	35.9%
Lymph-Popliteal R	3.1E-10	25.2%	1.2E-10	25.9%	8.2E-11	24.1%	1.7E-10	1.2E-10	70.0%
Lymph-Inguinal R	4.7E-09	3.5%	5.3E-09	3.1%	5.0E-09	4.3%	5.0E-09	2.7E-10	5.5%
Lymph-Inguinal L	4.8E-09	3.5%	5.5E-09	3.1%	5.2E-09	4.3%	5.2E-09	3.5E-10	6.7%
Lymph-Cubital R	4.7E-08	1.0%	5.4E-08	1.0%	5.3E-08	1.5%	5.1E-08	3.8E-09	7.3%
Lymph-Cubital L	5.3E-08	1.2%	6.3E-08	1.0%	5.5E-08	1.4%	5.7E-08	4.8E-09	8.4%
Lymph-Extrathoracic	8.1E-08	1.6%	9.7E-08	1.6%	8.5E-08	1.3%	8.7E-08	8.4E-09	9.6%
Lymph-Mesentery L	1.1E-07	0.2%	1.2E-07	0.2%	1.1E-07	0.4%	1.1E-07	6.5E-09	5.7%
Lymph-Mesentery R	1.2E-07	0.2%	1.2E-07	0.2%	1.1E-07	0.4%	1.1E-07	7.1E-09	6.2%
Lymph-Cervical	3.7E-07	0.2%	3.3E-07	0.2%	3.5E-07	0.3%	3.5E-07	2.0E-08	5.8%
Lymph-Axillary L	4.5E-07	0.6%	4.0E-07	0.6%	4.7E-07	0.7%	4.4E-07	3.9E-08	8.8%
Lymph-Breast L	5.0E-07	0.5%	5.2E-07	0.4%	4.8E-07	0.6%	5.0E-07	2.2E-08	4.3%
Lymph-Axillary R	5.2E-07	0.5%	4.6E-07	0.5%	5.3E-07	0.7%	5.0E-07	3.4E-08	6.7%
Lymph-Breast R	5.7E-07	0.5%	6.2E-07	0.4%	5.7E-07	0.6%	5.9E-07	3.1E-08	5.3%
Lymph-Thoracic U	8.1E-06	0.2%	8.5E-06	0.2%	8.3E-06	0.1%	8.3E-06	2.3E-07	2.7%
Lymph-Thoracic L	1.2E-02	0.0%	1.4E-02	0.0%	1.3E-02	0.0%	1.3E-02	9.0E-04	6.9%